American Society of Hematology
2021 L Street NW, Suite 900,
Washington, DC 20036
Phone: 202-776-0544 | Fax 202-776-0545
editorial@hematology.org

Structures of VWF tubules before and after concatemerization reveal a mechanism of disulfide bond exchange

Tracking no: BLD-2022-016467R1

Jacob Anderson (Harvard Medical School, United States) Jing Li (Harvard Medical School, United States) Timothy Springer (Harvard Medical School, United States) Alan Brown (Harvard Medical School, United States)

Abstract:
von Willebrand Factor (VWF) is an adhesive glycoprotein that circulates in the blood as disulfide-linked concatemers and functions in primary hemostasis. The loss of long VWF concatemers is associated with the excess bleeding of type 2A von Willebrand (VW) disease. Formation of the disulfide bonds that concatemerize VWF requires VWF to self-associate into helical tubules, yet how the helical tubules template intermolecular disulfide bonds is not known. Here, we report cryo-EM structures of complete VWF tubules before and after intermolecular disulfide-bond formation. The structures provide evidence that VWF tubulates through a charge-neutralization mechanism and that the A1 domain enhances tubule length by crosslinking successive helical turns. In addition, the structures reveal disulfide states prior to and after disulfide bond-mediated concatemerization. The structures and proposed assembly mechanism provide a foundation to rationalize VW disease-causing mutations.

Conflict of interest: No COI declared

COI notes:

Preprint server: No;

Author contributions and disclosures: J.R.A. collected and processed all electron microscopy data and built atomic models. J.L. purified proteins, performed light scattering experiments, and assembled tubules. T.A.S. and A.B. supervised the research. J.R.A., T.A.S., and A.B. wrote the paper with contributions from J.L.

Non-author contributions and disclosures: No;

Agreement to Share Publication-Related Data and Data Sharing Statement: Atomic models of VWF tubules formed with monomeric D1-A1 and dimeric D1-A1 have been deposited to the PDB with accession codes 8D3C and 8D3D, respectively. Composite maps for the VWF tubules formed with monomeric D1-A1 or dimeric D1-A1 have been deposited to the EMDB with accession codes EMD-27156 and EMD-27157, respectively. These density maps are composites derived from stitching together a central masked bead to create a tubule with length similar to the helical reconstruction. The unstitched map for the VWF tubule formed from dimeric D1-A2 has been deposited to the EMDB with accession code EMD-27158.

Clinical trial registration information (if any):

Structures of VWF tubules before and after concatemerization reveal a mechanism of disulfide bond exchange

Jacob R. Anderson[1,*], Jing Li[1,2,*], Timothy A. Springer[1,2,3†], Alan Brown[1†]

Running title: Structures of VWF tubules with the A1 domain

Affiliations:

[1]Department of Biological Chemistry and Molecular Pharmacology, Harvard Medical School, Boston, MA 02115, USA

[2]Program in Cellular and Molecular Medicine, Boston Children's Hospital, Boston, MA 02115, USA

[3]Department of Pediatrics, Harvard Medical School, Boston, MA 02115, USA

*Co-first authors

[†]Corresponding authors: springer@crystal.harvard.edu (T.A.S.) and alan_brown@hms.harvard.edu (A.B.)

This manuscript contains 4,272 words for the main text, 134 words for the abstract, 7 figures, 58 references, 5 supplementary figures and 3 supplementary tables.

Key points:

- Structures of VWF tubules identify the cysteine residues responsible for concatemerization and reveal a disulfide bond exchange mechanism
- The A1 domain promotes tubule length by linking helical turns in the VWF tubule

ABSTRACT

von Willebrand Factor (VWF) is an adhesive glycoprotein that circulates in the blood as disulfide-linked concatemers and functions in primary hemostasis. The loss of long VWF concatemers is associated with the excess bleeding of type 2A von Willebrand (VW) disease. Formation of the disulfide bonds that concatemerize VWF requires VWF to self-associate into helical tubules, yet how the helical tubules template intermolecular disulfide bonds is not known. Here, we report cryo-EM structures of complete VWF tubules before and after intermolecular disulfide-bond formation. The structures provide evidence that VWF tubulates through a charge-neutralization mechanism and that the A1 domain enhances tubule length by crosslinking successive helical turns. In addition, the structures reveal disulfide states prior to and after disulfide bond-mediated concatemerization. The structures and proposed assembly mechanism provide a foundation to rationalize VW disease-causing mutations.

INTRODUCTION

Von Willebrand (VW) disease is the most common bleeding disorder worldwide and is characterized by excessive bleeding due to mutations in the gene encoding von Willebrand factor (VWF)[1]. VWF is an adhesive multi-domain plasma glycoprotein (Figure 1A) that functions in hemostasis by acting as both a stabilizer of coagulation factor VIII and a crosslinker of platelets and extracellular-matrix components at sites of vascular injury. The ability of VWF to staunch bleeding is directly correlated with its ability to form long and polyvalent disulfide-linked concatemers[2]. Short VWF concatemers circulating in the blood are associated with the excess bleeding of type 2A VW disease[1]. Maturation of VWF requires a remarkable intracellular biogenesis pathway that includes the formation of intra- and intermolecular disulfide bonds, glycosylation, and proteolytic removal of an N-terminal D1D2 prodomain[3] (Figure 1A). Biogenesis starts in the endoplasmic reticulum (ER), where VWF dimerizes through disulfide bonds between C-terminal cysteine knot (CK) domains[4]. Surprisingly, however, the disulfide bonds that covalently link VWF dimers into concatemers do not form in the oxidoreductase-rich ER[3] but in the acidic environments of the *trans*-Golgi and Weibel-Palade bodies (WPBs)[5,6]. In these acidic environments, the C-terminal A2-CK domains in VWF zipper together to form a "dimeric bouquet[7] and the dimers then assemble through their N-terminal portions into helical tubules[8]. The helical tubules are proposed to template the formation of intermolecular disulfide bonds between adjacent D3 domains, leading to formation of VWF concatemers[9]. However, the mechanism by which tubules template concatemerization is incompletely understood and there is uncertainty about which cysteine residues form the intermolecular disulfide linkages. Mass spectrometry showed that C1099 and C1142 were free in monomeric VWF D′D3[10] but not in mature VWF[11]. Substitution of these two cysteine residues with alanine prevented disulfide-mediated dimerization of the D′D3 domain and concatemerization of full-

length VWF[10]. However, only C1142-C1142 linked peptides were observed in tryptic digests of plasma VWF[12]. Further casting doubt on the presence of a C1099-C1099 linkage was a recent cryo-EM structure of human MUC2, a filament-forming mucin with an N-terminal head domain that resembles VWF, which indicated that C1142 and C1097 but not C1099 are responsible for intermolecular disulfide bonds[13]. However, our previous crystal structure of monomeric VWF D′D3 showed that C1097 is engaged in an intradomain disulfide bond with C1091[14].

Here, we have determined cryo-EM structures of VWF helical tubules before and after intermolecular disulfide bond formation. The structures unambiguously identify the cysteine residues involved in concatemerization (C1142 and C1097) and reveal that tubulation templates concatemerization through a disulfide-bond exchange mechanism. We propose a detailed assembly pathway that explains the pH-dependence of tubule formation, the role of the A1 domain in stabilizing tubules, and how mutations associated with type 2A VW disease might impair VWF concatemerization by limiting tubule formation.

METHODS

Expression and purification of VWF proteins

Sequences encoding VWF D1-D3 (residues 1-1264), D1-A1 (1-1464), and D1-A2 (1-1671) with a C-terminal hexahistidine tag and a furin cleavage site mutated to ASAS were cloned into PD2529 vectors. Expi293 cells were transfected using FectoPRO (Polyplus, #101000014) in 1 L Expi293 medium. Valproic acid and glucose were added to the culture 24 hrs after transfection to final concentrations of 3 mM and 0.4%, respectively. Six days after transfection, secreted proteins were purified from the media by His-affinity in 20 mM Tris-HCl pH 8, 300 mM NaCl, and 10 mM $CaCl_2$. After affinity chromatography, the purified protein was dialyzed into low salt buffer (20 mM Tris-HCl pH 7.4, 50 mM NaCl, and 10 mM $CaCl_2$). Next, anion-exchange chromatography was performed by elution with linearly increasing amounts of high salt buffer (20 mM Tris-HCl pH 7.4, 1 M NaCl, and 10 mM $CaCl_2$). Final purification was size-exclusion chromatography with a Sepharose 6 column (Cytiva) in 10 mM HEPES, pH 7.4, 100 mM NaCl, and 10 mM $CaCl_2$. Protein purity was analyzed by SDS-PAGE (Figure S1A).

Dynamic light scattering (DLS)

VWF proteins (22.5 µL at 0.11 mg/mL) were spiked with 3 µL 1 M sodium cacodylate buffer at various pHs and incubated at 37°C for 24 hrs. Afterwards, samples were placed in a 384 well black clear bottom plate (Aurora Microplates, #ABM2-10100A). Measurements were taken on a DynaPro Plate Reader III (Wyatt Technology) at 0.1 µs intervals at 25°C. Average hydrodynamic radii were calculated using DYNAMICS (Wyatt Technology).

Negative-stain electron microscopy

VWF tubules (3 µL at 0.01-0.3 mg/mL) were deposited onto glow discharged (15 s at 30 mA voltage) grids (EMS, #CF200-Cu). After 1 minute, the grids were blotted with filter paper, washed twice with 3 µL of 1.5% uranyl formate, and blotted again. Grids were imaged on a Tecnai T12 microscope equipped with a Gatan UltraScan 895 camera. Particle lengths were measured using Fiji[15].

Cryo-EM sample preparation and data collection

VWF proteins at 0.6-1 mg/mL were incubated in sodium cacodylate buffer at pH 5.2, 10 mM $CaCl_2$, and 100 mM NaCl for 24 hrs to allow tubule formation. After incubation, 3 µL of protein was deposited onto gold R2/1 grids (Quantifoil, #Q325AR1-2nm) precoated with continuous carbon that had been glow discharged for 15 s at 30 mA. The grids were blotted with a blot force of 2-5 and a blot time of 2-5 s using a Vitrobot Mark IV (Thermo Fisher Scientific) at 4°C and 100% humidity before being plunged into liquid ethane.

Cryo-EM data collection and image processing

Cryo-EM data for VWF D1-A1 tubules were collected on a Titan Krios microscope (Thermo Fischer Scientific) with a K3 detector with a BioQuantum Energy Filter (Gatan). Cryo-EM data for D1-A2 VWF tubules were collected on a Talos Arctica microscope with a K3 detector. Parameters used during data collection are provided in Table S1. All movies were motion corrected using MotionCor2[16]. Contrast transfer function (CTF) parameters were estimated with CTFFIND4[17]. Particles were picked using crYOLO[18] and imported into RELION-3.1.3[19] or RELION-4.0[20]. Particles were extracted in 384 or 400-pixel boxes with an inter-box distance of 123 or 197 pixels, respectively. 2D and 3D classification was used to remove false positives and contaminants. 3D refinement was initiated using a cylindrical reference with dimensions obtained from ns-EM of *in-vitro* assembled VWF tubules[21]. 3D refinement for all datasets employed helical symmetry with initial twist of 83.3° and rise of 26.8 Å. CTF refinement and Bayesian polishing were used to improve map quality. Following helical processing, a binary mask, applied to a central "bead", yielded maps with resolutions of 3.1, 3.2, and 4.7 Å for the D1A1 monomer, D1A1 dimer, and D1A2 dimer, respectively. Processing schemes are provided in Figures S1-S2.

Model building and refinement

Maps were sharpened for model building and refinement using phenix.auto_sharpen[22]. Model building was initiated by placing atomic models of MUC2 (PDB: 6TM2)[13] and the VWF A1 domain (PDB: 1AUQ)[23] into the density using ChimeraX[24]. Residues were mutated, inserted, or deleted to build the

VWF polypeptide using Coot v.0.9.3[25]. Atomic models were refined in ISOLDE[26] and Phenix.real_space_refinement[27] with symmetry constraints and restraints on Ramachandran angles and secondary structure.

Data Sharing

Atomic models of VWF tubules formed with monomeric D1-A1 and dimeric D1-A1 have been deposited to the PDB with accession codes 8D3C and 8D3D, respectively. Composite maps for the VWF tubules formed with monomeric D1-A1 or dimeric D1-A1 have been deposited to the EMDB with accession codes EMD-27156 and EMD-27157, respectively. These density maps are composites derived from stitching together a central masked bead to create a tubule with length similar to the helical reconstruction. The unstitched map for the VWF tubule formed from dimeric D1-A2 has been deposited to the EMDB with accession code EMD-27158.

RESULTS

Cryo-EM reconstruction of VWF tubules

Prior work had shown that the VWF prodomain (D1D2) is essential for concatemerization[5,28,29] and that D1-D3 constructs are sufficient for VWF tubulation *in vitro*, although inclusion of the A1 domain led to longer tubules[21]. We therefore recombinantly expressed and purified human D1-A1 (the VWF "head") with the furin-cleavage site mutated to ASAS to prevent prodomain cleavage in human Expi293 cells (Figure 1A-B). As seen previously[30], the C-terminally truncated VWF purified as size-separable monomers and disulfide-linked dimers (Figure S1A). Using dynamic light scattering (DLS; Figure 1C) and negative-stain electron microscopy (ns-EM; Figure 1D-E), we demonstrated that the D1-A1 dimer could form tubules in low pH buffers containing calcium. We thus used pH 5.2 and 10 mM $CaCl_2$ to generate VWF tubules for cryo-EM analysis (Figure S1C). Using this sample, we were able to resolve the structure of the VWF tubule to 3.3-Å resolution (Figure 1F, Table S1, and Movie S1). The structure forms a 255-Å wide right-handed helix with an internal diameter of 145 Å. The overall dimensions, architecture, and helical parameters (83.3º twist and 26.8 Å rise) closely match cryo-ET reconstructions of VWF tubules inside WPBs[31], demonstrating that our *in-vitro* assembled tubules recapitulate native intracellular tubules.

Structure of a bead

Like reconstructions of VWF tubules at low resolution[21,31], we observed a repeating bead-like density (Figure 2A and Movie S1). Each bead has C2 symmetry and is formed by parts of four different VWF monomers (Figure 2B), while a single VWF monomer spans two beads (Figure 2C). Two antiparallel

D1D2 prodomains form the layer of the bead on the inner face of the tubule, while two D´D3 domains from neighboring molecules cradle between the D1 and D2 domains and form the outer layer of the bead (Figure 2B). A similar organization of D assemblies is found in MUC2[13]. The positioning of the two D3 domains atop the D1D2 cradle juxtaposes them for disulfide linkage to one another and explains the critical role of the prodomain in concatemerization[29].

The A1 domain is a VWF tubule constituent

Our structure revealed that the A1 domain, a globular domain of six amphipathic α-helices surrounding a hydrophobic six-stranded β-sheet core[23], locates to the outer tubule wall and participates in tubule packing by linking successive helical turns (Figure 3A). Specifically, each A1 domain makes *trans* interactions with E1, TIL2, and VWD2 domains of a VWF molecule in its own bead, as well as with a C8-1 domain four beads away in the next helical turn (consistent with the tubule having 4.2 beads per helical turn) (Figure 3B and Movie S1). Indeed, without the A1 domain there would be no contacts between neighboring turns of the tubule. To test the contribution of the A1 domain to tubule formation, we assessed the ability of a construct truncated at the end of the D3 domain to form tubules. As expected from prior work[21], loss of the A1 domain did not prevent tubule formation but led to significantly shorter tubules (Figures 3C, S2B). The involvement of the A1 domain in tubule packing and the promotion of long tubules may explain why D1-A1 constructs form longer WPB-like granules than D1-D3 constructs in cells[6].

We next aimed to exclude the possibility that the A2 domain might also contribute to tubule formation. To do this, we purified the dimeric form of the D1-A2 construct (Figures S1A, S2A) and showed using DLS and cryo-EM that it could form tubules, but with a mean length less than the D1-A1 construct (Figure S2B). Next, we determined a 4.8-Å resolution structure of tubules formed by the purified D1-A2 dimer (Figure S2C,D). The structure was nearly identical to the tubule formed with D1-A1 dimers (Figure S2E) and showed no additional density near the A1 domain that could correspond to the A2 domain (Figure S2F). This observation demonstrated that the A1 but not A2 domain is a structural component of the VWF helical tubule. In addition, the inability to resolve the A2 domain suggested that the 31-residues between the A1 and A2 domains form a flexible linker, in agreement with ns-EM of C-terminal VWF dimeric bouquets containing the A1 and A2 domains[7] and explaining the absence of density for the C-terminal portion of VWF in reconstructions of native VWF tubules in WPBs[31].

Structural basis for the pH-dependence of tubule formation

VWF tubulation is pH-dependent[21,32]. Histidine protonation has been implicated in this phenomenon based on histidine having a pKa (6.0) between the neutral pH of the ER and the acidic pH of the *trans*-Golgi and WPB[33]. One possible mechanism for pH-dependent tubulation is that protonated histidine sidechains form intermolecular salt bridges at acidic pH that stabilize the helical tubule. We therefore analyzed the 33 histidine residues that are resolved in our structure (Figure 4A, Table S2). First, we determined their conservation across VWF sequences[34]. Second, we calculated electrostatic potential and structure-based pKas for each histidine to determine which histidine residues are specifically protonated by a decrease in pH from 7.4 to 5.2. Third, we analyzed their location in the VWF tubule. This analysis revealed that only one histidine residue (H352) is in a potential interfacial salt bridge. Together with prior work showing substitution of H352 with an alanine did not impair VWF concatemerization[33], we conclude that interfacial salt bridges involving histidine residues are not required for VWF tubulation.

An alternative mechanism is that histidine protonation forms intramolecular salt bridges that stabilize a VWF conformation capable of self-associating into helical tubules. Evidence for this mechanism comes from our observation that H395, a highly conserved residue in the VWD2 domain, forms a potential salt bridge with D611 in the C8-2 domain that might lead to a tighter association of these domains at acidic pH than at a neutral pH (Figure 4B). Consistent with this model, a H395A substitution completely abolished VWF concatemerization[33]. H817 in the TIL´ domain also forms an apparent intramolecular salt bridge with E835 of the E´ domain (Figure 4C), which could potentially stabilize the bridge between neighboring beads.

Our structure also reveals a third possible mechanism for how acidic pH permits tubulation. When we analyzed the interfaces between VWF molecules, we found that most interfaces shared an electronegative charge at pH 7.4 (Figure 4D). Repulsion between these interfaces at neutral pH might prevent tubulation. We observed that several histidine residues occur within these electronegative environments - H421, H460, H556, and H817 (Figure 4E-G). This leads us to propose a charge-neutralization model; as the pH drops in the *trans*-Golgi, the electronegative charge is neutralized (Figure 4D) by histidine, aspartic acid, and glutamic acid protonation, allowing tubules to form. The charge neutralization model emphasizes that other residues besides histidine may regulate tubulation. Although we expected to see histidine residues in key interactions in tubules, we instead found that only a small number are found in such contacts, and these are restricted to intramolecular interfaces (Figure 4B, 4C). As pH is lowered in the *trans* and cis Golgi, it is not only histidine residues but also aspartic and glutamic acid residues that are protonated. The ratio of (Asp + Glu) : His residues in the D1-A1 domains is 5:1, and thus protonation of acidic residues may also have an important effect on tubulation.

Notably, the pI of the A1 domain (8.8) is substantially more basic than D1-D3 (pI 5.1). Charge neutralization by the A1 domain may therefore provide another mechanism by which the A1 domain promotes VWF tubulation. However, this effect is not essential to the core mechanism of tubulation because tubules can form in the absence of the A1 domain[21].

Identification of the disulfide-bonds required for concatemerization

The structure conclusively demonstrates that C1097 and C1142 in the D3 domain are responsible for the disulfide-mediated concatemerization of VWF (Figure 5A-C). Density shows that both residues form intermolecular disulfide bonds with their equivalent residues in the neighboring D3 domain (Figure S3A-B). Thus, VWF and MUC2 multimers are disulfide-bonded through equivalent cysteine residues[13]. We further observed that C1099, which was previously speculated to form an intermolecular disulfide bond[10], instead forms an intramolecular disulfide bond with C1091 (Figures 5B, S3C).

To observe the conformation of VWF prior to disulfide-linkage of D3 domains, we reconstituted VWF tubules with our monomeric D1-A1 construct for cryo-EM analysis (Figure S1D). VWF retained its monomeric form within these tubules (Figure S1B). This observation confirms that prior disulfide-mediated concatemerization is not a prerequisite for VWF tubulation[8]. From the monomer-derived VWF tubules, we obtained a 3.2-Å resolution structure which revealed no gross morphological changes and similar helical parameters to VWF tubules reconstituted with disulfide-linked dimers (Figure S2C-D). The only changes are at the interface between neighboring D3 domains (Figure 5A-F). In general, the D3 interface between monomers is less ordered than in the dimer-derived tubule, presumably due to increased flexibility caused by an absence of covalent linkages. Notable changes occur in the 910-923 and 1092-1098 loops (Figures 5F, S4A-C). Compared to before intersubunit disulfide bonding, the 910-923 loop shifts into a hydrophobic pocket of VWD3 (Figure S4A,B) and the 1092-1098 loop switches conformation (Figure S4C). The position of the 1092-1098 loop in the monomer-derived tubule matches the D´D3 monomer crystal structure[14]. However, the C1142-containing loop in the crystal structure adopts a different conformation from that observed in either tubule structure (Figure S4D). In the monomeric crystal structure, determined at mildly alkaline pH, the loop conformation buries C1142 in a hydrophobic pocket. This conformation would protect against premature disulfide bond formation in the ER.

The structure of the monomer-derived tubule confirms that C1099 and C1142 are unpaired (Figure S3D,E) as expected from their ability to be alkylated in purified monomers[10]. In contrast to their disulfide-bonded state in the dimer-derived tubules, the sulfhydryl groups from neighboring C1142

residues are clearly unbonded (Figure 5E, S3E). C1097, the other residue responsible for VWF concatemerization, is confirmed to be in an intramolecular disulfide bond with C1091 (Figure 5D, S3F), as observed in the D´D3 monomer crystal structure[14].

VWF concatemerizes through a disulfide exchange mechanism

The observation that C1097 forms an intramolecular disulfide bond prior to concatemerization but an intermolecular disulfide bond in the concatemer confirmed our hypothesis that VWF concatemerization proceeds through a disulfide-bond exchange mechanism[14]. The details of this mechanism remain to be defined; however, we can rule out a suggestion that the D1 or D2 assemblies of VWF are oxidoreductases[35]. This proposal was based on the presence of CXXC sequences in both the prodomain and in the active site sequence of oxidoreductase family members, and that insertion of a single glycine into CXXC motifs in either the D1 or D2 assemblies inhibited VWF concatemerization[35]. However, there is no overall structural homology between VWF D assemblies and oxidoreductases. Furthermore, the cysteine residues in these motifs are disulfide bonded in the VWF monomer and greater than 35 Å from the disulfide bonds at the D3:D3 interface (Figure S5A-C).

Interestingly, we observed additional density extending from the sulfhydryl group of unpaired C1099 in the monomer-derived tubule (Figure S3D) that could correspond to S-glutathionylation or formation of a disulfide with a component of the culture medium such as cysteine during D1-A1 protein production.

Disease mechanisms

The loss of ultralong VWF concatemers in type 2A VW disease results from impaired intracellular multimerization of VWF or increased susceptibility of secreted VWF to proteolysis by ADAMTS13. Our structures provided an opportunity to interpret, at the atomic level, a well-annotated list of clinical mutations[36] (Figure 6A, Table S3). We focused on Type 2A VW disease mutations that did not substitute cysteine residues, which likely affect VWF folding by disrupting normal disulfide-bonding. We note that several non-cysteine mutations map to interfaces between neighboring molecules including Y87S and R202W. The Y87S mutation has been shown to disrupt tubular packing and block concatemerization[6,37]. Y87 lines a crevice in the VWD1 domain into which an α-helix protrudes from the C8-2 domain of a neighboring molecule (Figure 6B). The Y87S substitution would admit solvent and destabilize this packing interaction, potentially causing decreased tubule formation. R202 sits at the nexus between three VWF molecules at the interface between beads and forms both cation-π interactions (with Y730 of the neighboring E2 domain) and electrostatic interactions with D168 and D434 (Figure 6C). Substitution to

tryptophan[38] (R202W) would disrupt these interactions, consistent with our model that charge neutralization is required for effective tubulation.

A number of type 2A VW disease mutations with unknown pathomechanisms map to the A1 domain (Figure 6D, Table S3). Our observation that the A1 domain is a constituent of the tubule wall and enhances tubule length *in vitro* (Figure S3C) suggests that mutations that impair the stability of the A1 domain might limit VWF concatemerization by generating short tubules. Consistent with this model, the VW disease-associated L1307P substitution, which inserts a proline into the hydrophobic core of the A1 domain, has short and round WPB-like granules in cells that are indicative of reduced VWF tubule length[39]. L1276P likely functions through a similar mechanism by disrupting the β1 strand of A1[40] (Figure 6D).

DISCUSSION

Here, we have leveraged the propensity of C-terminally truncated VWF constructs to form tubules *in vitro* to determine structures of VWF before and after disulfide-bond formation between D3 domains. These structures, together with prior information, allow us to generate a multi-step model for the assembly of full-length VWF into concatemers (Figure 7).

Although our structures were generated from N-terminal domains only, a process of elimination can be used to determine which VWF molecules belong to the same C-terminally linked dimer *in vivo*. We can exclude the subunits that contribute D3 domains to a single bead (Figure 7A, Option I), as their disulfide bonding would generate a closed dimer. We can also exclude the two subunits that contribute prodomains to a single bead (Option II) because their extended and antiparallel configuration places their A1 domains 22 nm apart, which is more than twice the distance between A2 domains in the dimeric A1-CK bouquet[7]. It is unlikely that this distance can be bridged by the 31-residue flexible linker between the A1 and A2 domains. Similarly, the distance between A1 domains makes Option III unlikely. Instead, we propose that the dimer corresponds to symmetry related subunits with prodomains in adjacent beads (Option IV), where the 10-nm distance between A1 domains matches the distance between A2 domains in the dimeric A1-CK bouquet[7].

The interface between VWF monomers in the most feasible model for linking dimeric bouquets (option IV) is ~8,830 Å^2, more than 5x larger than in alternative models (Fig. 7A). This large size makes it highly preferred over the alternatives[41]. Notably, this dimer is also domain swapped, i.e. D3 of one monomer in the dimeric bouquet is nestled in the D1-D2 cradle of the other monomer (Fig. 7A and B). Domain

swapping was also seen in MUC2 filaments[13] and occurs because the connection between the D2 domain and the D' domain is shorter in the extended conformation of the D1-D3 unit shown in Fig. 7A than it would be if the monomer doubled back to allow its own D3 to interact with D1-D2.

A consequence of the intertwined, domain-swapped arrangement is that the two D3 domains from a single dimer are kept apart (with ~17 nm between equivalent C1142 residues), thereby preventing closed dimer formation. Noncovalent association of the VWF heads in this manner would also reduce the risk of heads from the same dimer becoming incorporated into different tubules, which would lead to tubule bundling inconsistent with the regularly aligned arrangement of VWF tubules in WPBs[42]. It is for these reasons that we hypothesize that noncovalent head pairing occurs as a discrete step before tubule formation. Intradimer head pairing could be the major pH-regulated step that once formed is sufficient for tubule formation. However, histidine residues experimentally important for tubule formation[33] (e.g. H95 and H737) are found outside the putative intradimer interface as well as within it (H395, H460 and H817) (Table S2), implying that head pairing alone may not fully explain the pH dependence of tubule formation.

Having rationalized the C-terminally linked VWF dimer in the VWF tubule, we propose a model (Figure 7B) wherein the first step of VWF maturation after leaving the ER is zippering together of the C-terminal A2-CK domains into a dimeric bouquet[7]. We propose that two dimeric bouquets next associate through their N-terminal heads to form helical tubules. In our model, the pairing of C-terminally disulfide-linked dimers through their N-terminal heads recruits additional dimers through D1-A1 interactions to form a tubule that can polymerize at either tubule end. The dimerized A2-CK tails would spiral outwards from the central tubule, but with sufficient flexibility conferred by the A1-A2 linker to not be seen in tomographic reconstructions[31]. The A1 domain crosslinks successive helical turns; a property that likely compacts and rigidifies the tubule, explaining how the A1 domain promotes increased tubule length[21] (Figure 3C), and why some mutations within the A1 domain cause type 2A VW disease through the loss of ultralong concatemers.

A consequence of tubule formation is that D3 domains from neighboring dimers are brought sufficiently close to allow intersubunit disulfide bonding. We show that disulfide bonding must occur through a disulfide-bond exchange mechanism as one of the paired cysteines, C1097, is initially in an intramolecular disulfide bond with C1091. C1099 is likely critical to this reshuffling as it eventually becomes paired with C1091 after intersubunit disulfide bonding. We propose that nucleophilic attack by C1099 on the C1091-C1097 disulfide liberates C1097 for formation of the C1097-C1097' disulfide in

concatemers as previously proposed[43] (Figure 7B). The disulfide linkage between C1142 residues is promoted by their close juxtaposition in the tubule arrangement and can occur without disulfide exchange. Further work will be required to clarify a more detailed mechanism, including identifying which enzymes or small molecules act as electron acceptors for the cysteine sulfhydryl groups. With its D3 disulfide bonds formed, VWF is stored in WPBs. During secretion, the pH in WPBs rises to that in the bloodstream, allowing VWF tubules to uncoil, during which the mature VWF concatemer and the cleaved prodomain dissociate.

While preparing this manuscript, two other groups reported cryo-EM structures of short VWF tubules reconstituted *in vitro* from D1D2 prodomains and dimeric D′D3[44–46]. These reports agree with our assignment of the cysteines responsible for VWF concatemerization. However, without the stabilization provided by the A1 domain, their tubules contained only a few helical turns. A key finding from our study is that the A1 domain plays a structural role in VWF concatemerization, suggesting that type 2A mutations within the A1 domain may cause defective concatemer genesis.

In conclusion, we elucidate key steps in VWF biogenesis through cryo-EM structures of VWF tubules before and after intermolecular disulfide-bond formation. From these structures we present a model for how charge-neutralization in the acidic environment of the *trans*-Golgi allows tubule formation in which the D3 domains are juxtaposed for disulfide bonding through a disulfide-bond exchange mechanism.

ACKNOWLEDGMENTS

Cryo-EM data were collected at The Harvard Cryo-EM Center for Structural Biology. We thank Sarah Sterling, Richard Walsh, and Shaun Rawson for microscopy and computing assistance. J.R.A., T.A.S. and A.B. are supported by grants from the National Institute of Health (F30-HL162128, R01-HL148755 and R01-GM141109, respectively). A.B. is a Pew Scholar.

AUTHOR CONTRIBUTIONS

J.R.A. collected and processed all electron microscopy data and built atomic models. J.L. purified proteins, performed light scattering experiments, and assembled tubules. T.A.S. and A.B. supervised the research. J.R.A., T.A.S., and A.B. wrote the paper with contributions from J.L.

DECLARATION OF INTERESTS

Authors declare that they have no competing interests.

REFERENCES

1. Leebeek FWG, Eikenboom JCJ. Von Willebrand's Disease. *N Engl J Med*. 2016;375(21):2067–2080.

2. Federici AB, Bader R, Pagani S, et al. Binding of von Willebrand factor to glycoproteins Ib and IIb/IIIa complex: affinity is related to multimeric size. *Br J Haematol*. 1989;73(1):93–99.

3. Wagner DD, Marder VJ. Biosynthesis of von Willebrand protein by human endothelial cells. Identification of a large precursor polypeptide chain. *J. Biol. Chem.* 1983;258(4):2065–2067.

4. Marti T, Rösselet SJ, Titani K, Walsh KA. Identification of disulfide-bridged substructures within human von Willebrand factor. *Biochemistry*. 1987;26(25):8099–8109.

5. Mayadas TN, Wagner DD. In vitro multimerization of von Willebrand factor is triggered by low pH. Importance of the propolypeptide and free sulfhydryls. *J. Biol. Chem.* 1989;264(23):13497–13503.

6. Michaux G, Abbitt KB, Collinson LM, et al. The physiological function of von Willebrand's factor depends on its tubular storage in endothelial Weibel-Palade bodies. *Dev. Cell*. 2006;10(2):223–232.

7. Zhou Y-F, Eng ET, Nishida N, et al. A pH-regulated dimeric bouquet in the structure of von Willebrand factor. *EMBO J*. 2011;30(19):4098–4111.

8. Wagner DD, Saffaripour S, Bonfanti R, et al. Induction of specific storage organelles by von Willebrand factor propolypeptide. *Cell*. 1991;64(2):403–413.

9. Springer TA. von Willebrand factor, Jedi knight of the bloodstream. *Blood*. 2014;124(9):1412–1425.

10. Purvis AR, Gross J, Dang LT, et al. Two Cys residues essential for von Willebrand factor multimer assembly in the Golgi. *Proc. Natl. Acad. Sci. U.S.A.* 2007;104(40):15647–15652.

11. Legaz ME, Schmer G, Counts RB, Davie EW. Isolation and characterization of human Factor VIII (antihemophilic factor). *J. Biol. Chem.* 1973;248(11):3946–3955.

12. Dong Z, Thoma RS, Crimmins DL, et al. Disulfide bonds required to assemble functional von Willebrand factor multimers. *J. Biol. Chem.* 1994;269(9):6753–6758.

13. Javitt G, Khmelnitsky L, Albert L, et al. Assembly Mechanism of Mucin and von Willebrand Factor Polymers. *Cell*. 2020;183(3):717-729.e16.

14. Dong X, Leksa NC, Chhabra ES, et al. The von Willebrand factor D'D3 assembly and structural principles for factor VIII binding and concatemer biogenesis. *Blood*. 2019;133(14):1523–1533.

15. Schindelin J, Arganda-Carreras I, Frise E, et al. Fiji: an open-source platform for biological-image analysis. *Nat. Methods*. 2012;9(7):676–682.

16. Zheng SQ, Palovcak E, Armache J-P, et al. MotionCor2: anisotropic correction of beam-induced motion for improved cryo-electron microscopy. *Nat. Methods*. 2017;14(4):331–332.

17. Rohou A, Grigorieff N. CTFFIND4: Fast and accurate defocus estimation from electron micrographs. *J Struct Biol*. 2015;192(2):216–221.

18. Wagner T, Lusnig L, Pospich S, et al. Two particle-picking procedures for filamentous proteins: SPHIRE-crYOLO filament mode and SPHIRE-STRIPER. *Acta Crystallogr D Struct Biol*. 2020;76(Pt 7):613–620.

19. Zivanov J, Nakane T, Forsberg BO, et al. New tools for automated high-resolution cryo-EM structure determination in RELION-3. *elife*. 2018;7:163.

20. Kimanius D, Dong L, Sharov G, Nakane T, Scheres SHW. New tools for automated cryo-EM single-particle analysis in RELION-4.0. *Biochem. J.* 2021;478(24):4169–4185.

21. Huang R-H, Wang Y, Roth R, et al. Assembly of Weibel-Palade body-like tubules from N-terminal domains of von Willebrand factor. *Proc. Natl. Acad. Sci. U.S.A.* 2008;105(2):482–487.

22. Terwilliger TC, Sobolev OV, Afonine PV, Adams PD. Automated map sharpening by maximization of detail and connectivity. *Acta Crystallogr D Struct Biol*. 2018;74(Pt 6):545–559.

23. Emsley J, Cruz M, Handin R, Liddington R. Crystal structure of the von Willebrand Factor A1 domain and implications for the binding of platelet glycoprotein Ib. *J. Biol. Chem.* 1998;273(17):10396–10401.

24. Pettersen EF, Goddard TD, Huang CC, et al. UCSF ChimeraX: Structure visualization for researchers, educators, and developers. *Protein Sci.* 2021;30(1):70–82.

25. Brown A, Long F, Nicholls RA, et al. Tools for macromolecular model building and refinement into electron cryo-microscopy reconstructions. *Acta Crystallogr. D Biol. Crystallogr.* 2015;71(Pt 1):136–153.

26. Croll TI. ISOLDE: a physically realistic environment for model building into low-resolution electron-density maps. *Acta Crystallogr D Struct Biol*. 2018;74(Pt 6):519–530.

27. Afonine PV, Poon BK, Read RJ, et al. Real-space refinement in PHENIX for cryo-EM and crystallography. *Acta Crystallogr D Struct Biol*. 2018;74(Pt 6):531–544.

28. Verweij CL, Hart M, Pannekoek H. Expression of variant von Willebrand factor (vWF) cDNA in heterologous cells: requirement of the pro-polypeptide in vWF multimer formation. *EMBO J.* 1987;6(10):2885–2890.

29. Wise RJ, Pittman DD, Handin RI, Kaufman RJ, Orkin SH. The propeptide of von Willebrand factor independently mediates the assembly of von Willebrand multimers. *Cell*. 1988;52(2):229–236.

30. Purvis AR, Sadler JE. A covalent oxidoreductase intermediate in propeptide-dependent von Willebrand factor multimerization. *J. Biol. Chem.* 2004;279(48):49982–49988.

31. Berriman JA, Li S, Hewlett LJ, et al. Structural organization of Weibel-Palade bodies revealed by cryo-EM of vitrified endothelial cells. *Proc. Natl. Acad. Sci. U.S.A.* 2009;106(41):17407–17412.

32. Wagner DD, Mayadas T, Marder VJ. Initial glycosylation and acidic pH in the Golgi apparatus are required for multimerization of von Willebrand factor. *J. Cell Biol.* 1986;102(4):1320–1324.

33. Dang LT, Purvis AR, Huang R-H, Westfield LA, Sadler JE. Phylogenetic and functional analysis of histidine residues essential for pH-dependent multimerization of von Willebrand factor. *J. Biol. Chem.* 2011;286(29):25763–25769.

34. Glaser F, Pupko T, Paz I, et al. ConSurf: identification of functional regions in proteins by surface-mapping of phylogenetic information. *Bioinformatics*. 2003;19(1):163–164.

35. Mayadas TN, Wagner DD. Vicinal cysteines in the prosequence play a role in von Willebrand factor multimer assembly. *Proc. Natl. Acad. Sci. U.S.A.* 1992;89(8):3531–3535.

36. Hampshire DJ, Goodeve AC. The international society on thrombosis and haematosis von Willebrand disease database: an update. *Semin Thromb Hemost*. 2011;37(5):470–479.

37. Rosenberg JB, Haberichter SL, Jozwiak MA, et al. The role of the D1 domain of the von Willebrand factor propeptide in multimerization of VWF. *Blood*. 2002;100(5):1699–1706.

38. Baronciani L, Federici AB, Punzo M, et al. Type 2A (IIH) von Willebrand disease is due to mutations that affect von Willebrand factor multimerization. *J Thromb Haemost*. 2009;7(7):1114–1122.

39. Wang J-W, Bouwens EAM, Pintao MC, et al. Analysis of the storage and secretion of von Willebrand factor in blood outgrowth endothelial cells derived from patients with von Willebrand disease. *Blood*. 2013;121(14):2762–2772.

40. Meyer D, Fressinaud E, Gaucher C, et al. Gene defects in 150 unrelated French cases with type 2 von Willebrand disease: from the patient to the gene. INSERM Network on Molecular Abnormalities in von Willebrand Disease. *Thromb Haemost*. 1997;78(1):451–456.

41. Krissinel E, Henrick K. Inference of macromolecular assemblies from crystalline state. *Journal of Molecular Biology*. 2007;372(3):774–797.

42. Streetley J, Fonseca A-V, Turner J, et al. Stimulated release of intraluminal vesicles from Weibel-Palade bodies. *Blood*. 2019;133(25):2707–2717.

43. Dong X, Springer TA. Disulfide exchange in multimerization of von Willebrand factor and gel-forming mucins. *Blood*. 2021;137(9):1263–1267.

44. Shu Z, Zeng J, Xia L, Cai H, Zhou A. Structural mechanism of VWF D'D3 dimer formation. *Cell Discov*. 2022;8(1):14–4.

45. Zeng J, Shu Z, Liang Q, et al. Structural basis of Von Willebrand Factor multimerization and tubular storage. *Blood*. 2022;

46. Javitt G, Fass D. Helical self-assembly of a mucin segment suggests an evolutionary origin for von Willebrand factor tubules. *Proc National Acad Sci*. 2022;119(15):e2116790119.

47. Ashkenazy H, Abadi S, Martz E, et al. ConSurf 2016: an improved methodology to estimate and visualize evolutionary conservation in macromolecules. *Nucleic Acids Research*. 2016;44(W1):W344-50.

48. Jurrus E, Engel D, Star K, et al. Improvements to the APBS biomolecular solvation software suite. *Protein Sci.* 2018;27(1):112–128.

49. Allen S, Abuzenadah AM, Hinks J, et al. A novel von Willebrand disease-causing mutation (Arg273Trp) in the von Willebrand factor propeptide that results in defective multimerization and secretion. *Blood*. 2000;96(2):560–568.

50. Haberichter SL, Budde U, Obser T, et al. The mutation N528S in the von Willebrand factor (VWF) propeptide causes defective multimerization and storage of VWF. *Blood*. 2010;115(22):4580–4587.

51. Schneppenheim R, Thomas KB, Krey S, et al. Identification of a candidate missense mutation in a family with von Willebrand disease type IIC. *Hum. Genet.* 1995;95(6):681–686.

52. Brehm MA, Obser T, Budde U, Blood SS, 2012. Subcellular Localization of Von Willebrand Factor Mutants Correlates with Particular VWF Multimer Patterns. *Blood*. 2012;120(21):98.

53. Michiels JJ, Smejkal P, Moore G, Budde U. Combined use of rapid von Willebrand factor (VWF) activity, VWF-propetide and classical VWF assays for improved diagnosis of von Willebrand disease type 1, 2N …. *Thromb Haemost Res*. 2019;3(2):.

54. James PD, O'Brien LA, Hegadorn CA, et al. A novel type 2A von Willebrand factor mutation located at the last nucleotide of exon 26 (3538G>A) causes skipping of 2 nonadjacent exons. *Blood*. 2004;104(9):2739–2745.

55. Corrales I, Ramírez L, Altisent C, Parra R, Vidal F. Rapid molecular diagnosis of von Willebrand disease by direct sequencing. Detection of 12 novel putative mutations in VWF gene. *Thromb Haemostasis*. 2009;101(03):570–576.

56. Jackson SC, Sinclair GD, Cloutier S, et al. The Montreal platelet syndrome kindred has type 2B von Willebrand disease with the VWF V1316M mutation. *Blood*. 2009;113(14):3348–3351.

57. Casari C, Berrou E, Lebret M, et al. von Willebrand factor mutation promotes thrombocytopathy by inhibiting integrin αIIbβ3. *J. Clin. Invest.* 2013;123(12):5071–5081.

58. Castaman G, Eikenboom JC, Rodeghiero F, Briët E, Reitsma PH. A novel candidate mutation (Arg611-->His) in type I "platelet discordant" von Willebrand's disease with desmopressin-induced thrombocytopenia. *Br J Haematol*. 1995;89(3):656–658.

FIGURE LEGENDS

Figure 1. **Structure of a von Willebrand Factor (VWF) tubule**. **A**. Schematic of the domain organization of the VWF proprotein. Each D assembly except D´ is made of domains VWD (von Willebrand factor type D domain), C8, TIL (trypsin inhibitor-like cysteine rich domain), and E. D1 and D2 form a prodomain that is cleaved by furin protease before secretion. **B**. Strategy to obtain VWF monomers and disulfide-linked dimers. VWF D1-A1 was expressed in Expi293 cells and purified from the media as monomers and disulfide-linked dimers. The furin cleavage site was mutated to ASAS to prevent prodomain dissociation. **C**. Dynamic light scattering (DLS) experiments of purified D1-A1 incubated at indicated pH showing an increase in average hydrodynamic radius with a decrease in pH. Error bars represent difference of the means from two replicates. **D**. Representative micrographs from negative-stain electron microscopy showing VWF dimers incubated at pH 7.4 and 5.2 (scale bars are 50 nm). **E**. Quantification of panel D showing particle lengths measured from 3 micrographs from samples incubated together overnight. The bottom, middle, and top lines of the shaded boxes represent the first quartile, the median, and third quartile of measured particle length, respectively. The length of the whiskers below and above the box plot represent the lesser of the range of data or 1.5 multiplied by the interquartile range. **F**. Schematic and cryo-EM structure of the dimer-derived tubule showing the bead-like arrangement. The structure forms a right-handed helix with a helical rise of 26.8 Å and a helical twist of 83.3°. The cryo-EM map has been Gaussian filtered for visualization.

Figure 2. Organization of VWF within a tubule. **A**. Cryo-EM map of the dimer-derived VWF tubule in gray with a single bead colored by each of the four monomeric VWF subunits from which it is formed. Beads have two-fold symmetry. **B**. A single bead. The left view has the same orientation as in (A) and has a red dashed line separating symmetrical halves. The right view shows the luminal facing portion of the bead, which is formed by two antiparallel D1D2 prodomains that form a cradle for the binding of two juxtaposed D´D3 domains. **C**. A VWF monomer, colored by module, adopts an extended conformation that spans two beads. The D1D2 prodomain is in one bead, and the D´D3 and A1 domains are in a neighboring bead. Domains of neighboring VWF molecules are colored gray and are shown with thinner loops, helices, and strands.

Figure 3. The A1 domain is a component of the tubule and links helical repeats. **A**. Cryo-EM map of the dimer-derived VWF tubule in gray with A1 domains in pink. A single A1 domain is boxed together with the domains of the neighboring molecules with which it interacts. **B**. Details of the *trans* interactions an A1 domain makes with two neighboring VWF molecules. Distinct molecules are denoted by no

apostrophe, one apostrophe (’), or two apostrophes (’’). **C**. Quantification of tubule length observed by negative-stain electron microscopy with and without the A1 domain. Particle lengths measured from 3 micrographs from samples incubated together overnight. Whisker plots are as described in the Fig. 1E legend.

Figure 4. **Structural basis for pH-dependent VWF tubule formation**. **A**. The Cα positions of the 33 histidine residues resolved in the structure are depicted as spheres color coded based on sequence conservation obtained from 140 homologs using the ConSurf server[47]. **B**. Details of the intramonomer salt bridge made by H395. **C**. Details of the intramonomer salt bridge made by H817. **D**. Interface between D2-D3 of one molecule (denoted D2-1 and D3-1; grey) and the D2 domain of another molecule (D2-2; teal) (top). The interfaces are separated and colored by electrostatic potential calculated at pH 7.4 (middle) and 5.2 (bottom). Electrostatic potentials were calculated using the default coulombic parameters in ChimeraX 1.3[24]. The positions of surface-exposed histidine residues are marked with a black circle or a yellow star if highlighted in panels E-G. **E-G**. Examples of histidine residues - H421 (panel E), H556 and H817 (F) and H460 (G) - that change protonation state upon pH change from 7.4 to 5.2 in electronegative local environments.

Figure 5. **VWF concatemerization proceeds through a disulfide-exchange mechanism**. **A**. Overview showing the juxtaposition of domains D′-A1 from separate molecules in the center of a single bead. **B-C**. Arrangement of intra- and intermolecular disulfide bonds in VWF tubules generated with dimeric D1-A1. **D-E**. Arrangement of interfacial cysteines and intramolecular disulfide in VWF tubules generated with monomeric D1-A1. **F.** Superposition of D3 domains showing the rearrangement of the 1091-1097 loop between monomer and dimer states. Model superposition was performed using the matchmake function of ChimeraX.

Figure 6. **Type 2A mutations**. **A**. Positions of VW disease type 2A missense mutations mapped onto the structure of VWF D1-A1 as it occurs in a tubule. **B**. Y87 lines a crevice in the VWD1 domain. The type 2A VW disease mutation Y87S would allow solvent into this crevice, potentially disrupting tubule formation. **C**. R202 forms intra and intermolecular interactions with two additional VWF molecules denoted in purple and dark teal. R202W, a mutation causing type 2A VW disease, would disrupt these interactions. A dashed green line shows a π-cation bond. **D**. A1 domain in light pink with residues altered in type 2A VW disease colored in dark pink. Leucine residues described in the text are labeled.

Figure 7. **Model for VWF tubule assembly**. **A**. Options I-IV show the possible molecules that could be disulfide bonded at their C-termini in native tubules generated with full-length VWF. Distances between A1 domains (calculated between A1464 Cα positions) are shown below, together with surface representations of potential C-terminally linked dimers and their quantified interfacial surface area. An overview is provided with a single bead denoted with a dashed white outline. Interfacial surface areas were calculated using PDBePISA[41]. **B**. Schematic showing a hypothetical maturation pathway for full-length VWF based on our cryo-EM structures and prior work. In this model, the acidic environment of the Golgi induces two changes in the VWF dimer: the A2-CK domains zipper together and the N-terminals heads form a "dimer swapped" conformation with D3 of one monomer nestling in a D1-D2 cradle of the other monomer. N-terminal dimer association leads to tubule assembly. Within the tubule, D3 domains from different dimers are juxtaposed. Once positioned, a disulfide exchange occurs where C1097 is liberated from an intramolecular disulfide bond to form one of two disulfides that concatemerize VWF dimers at their D3 domain. The second disulfide, between adjacent C1142 residues, occurs without disulfide exchange. With dimers linked at their D3 domains, the VWF tubule can unfurl into a high molecular weight VWF concatemer upon exocytosis into blood plasma.

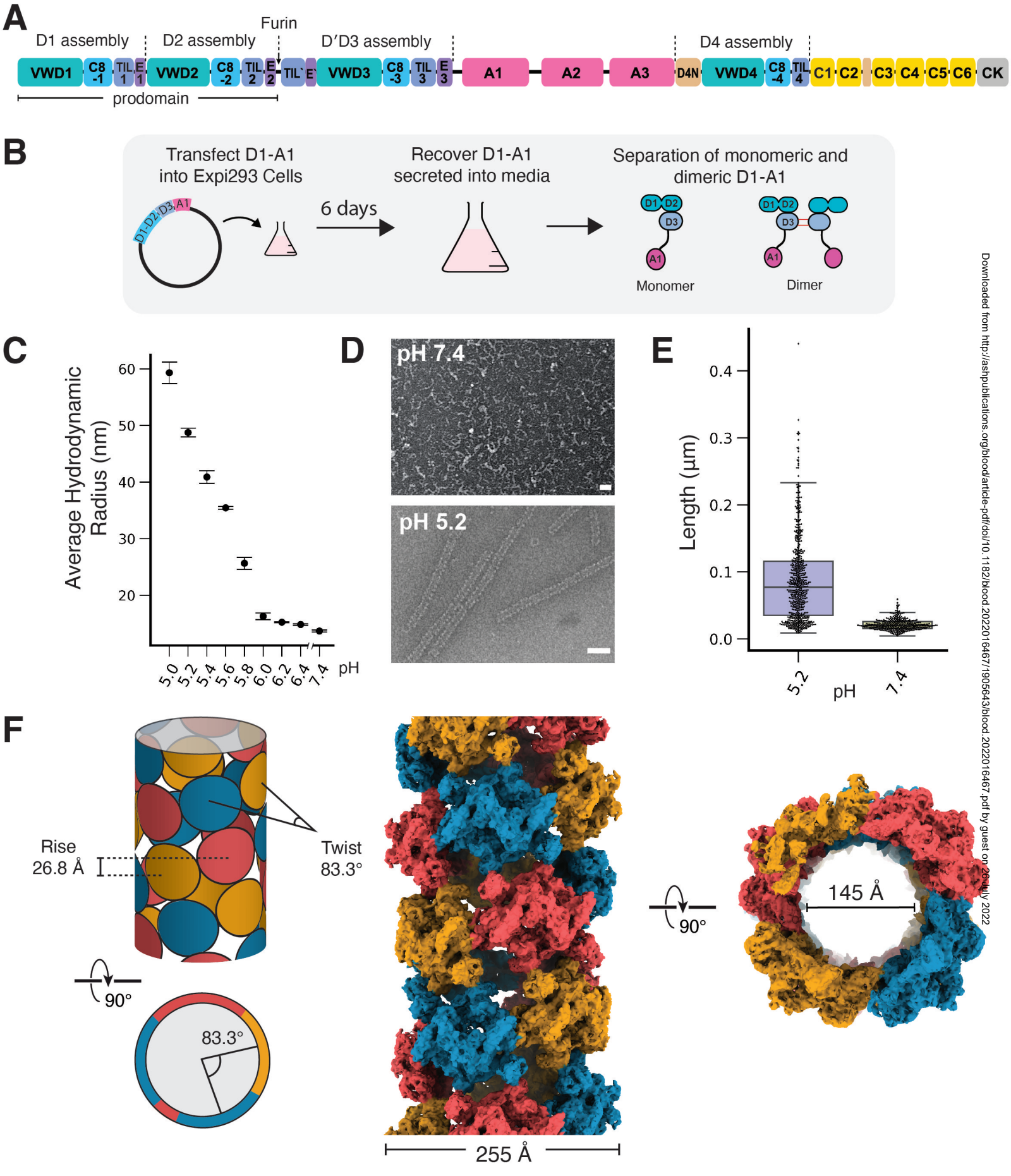

Figure 2

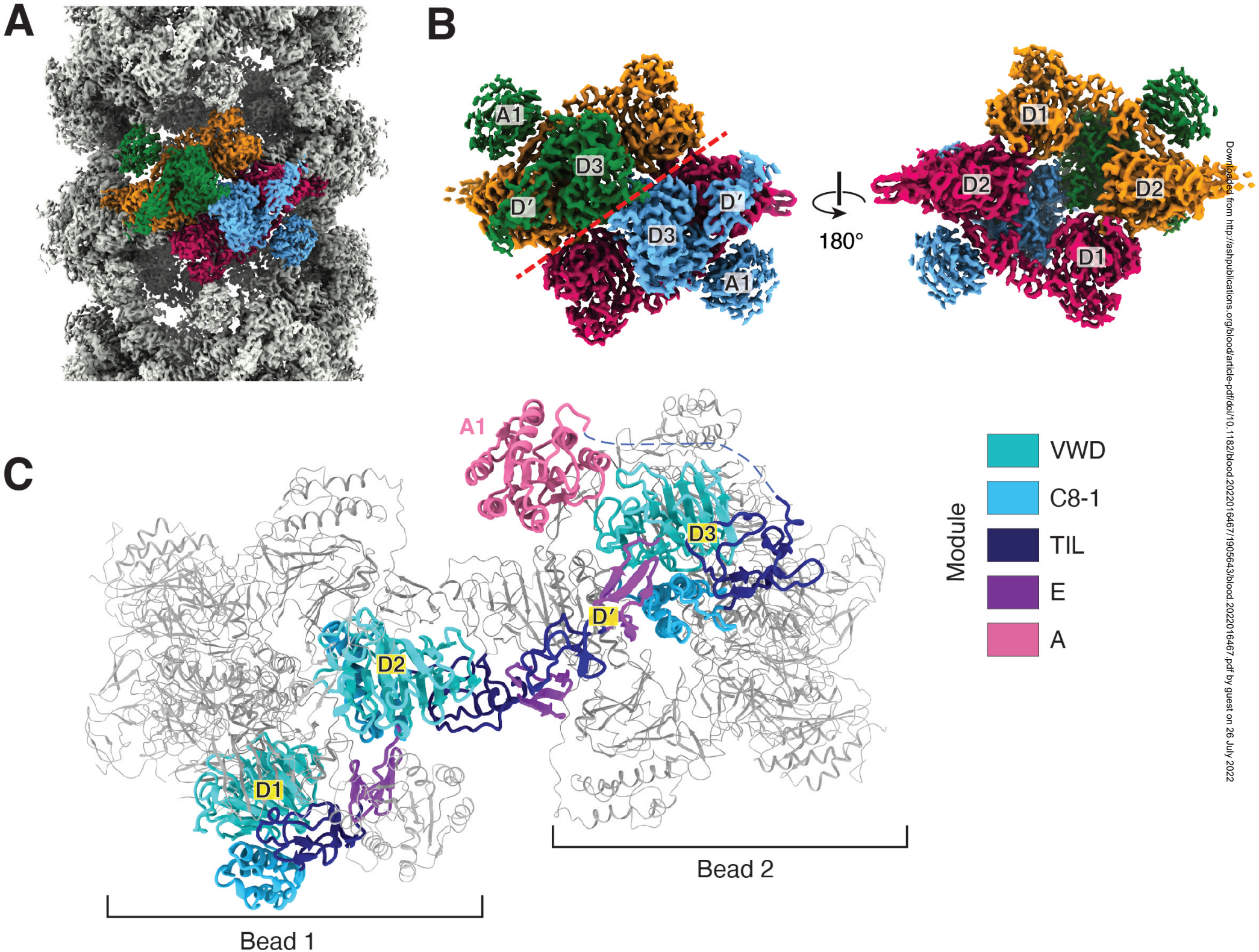

Figure 3

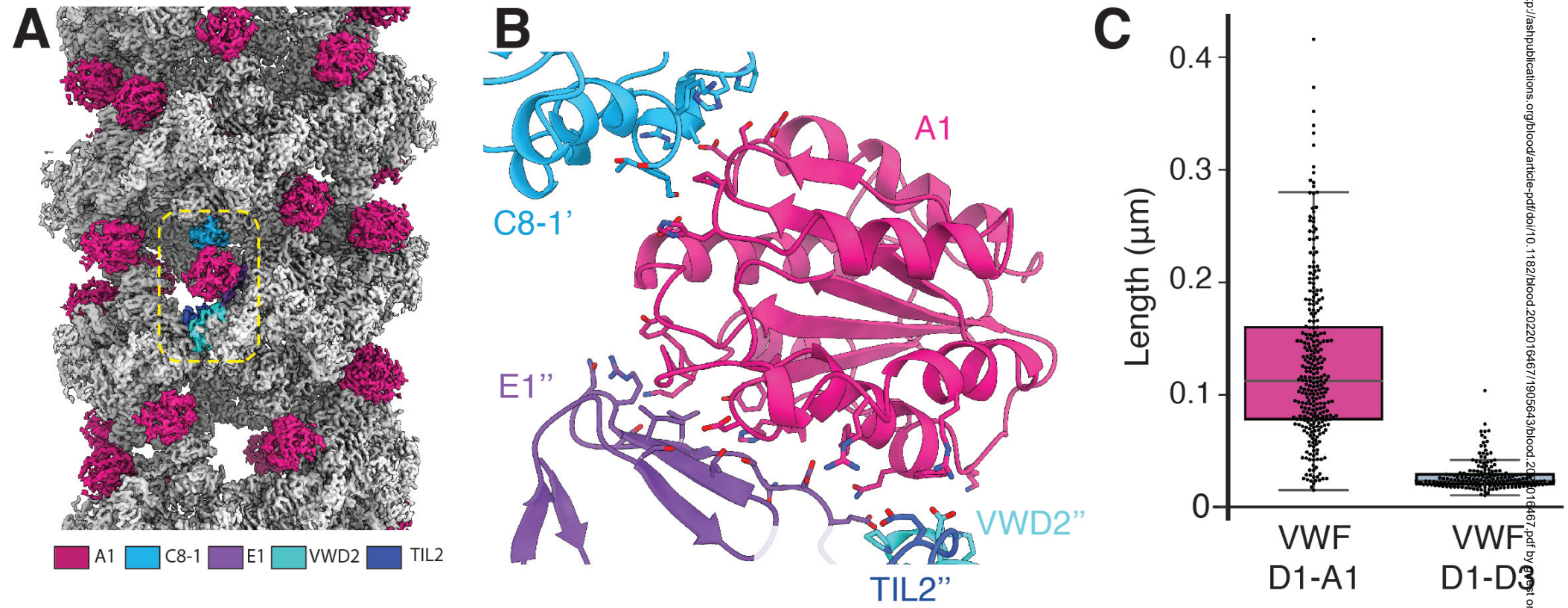

Figure 4

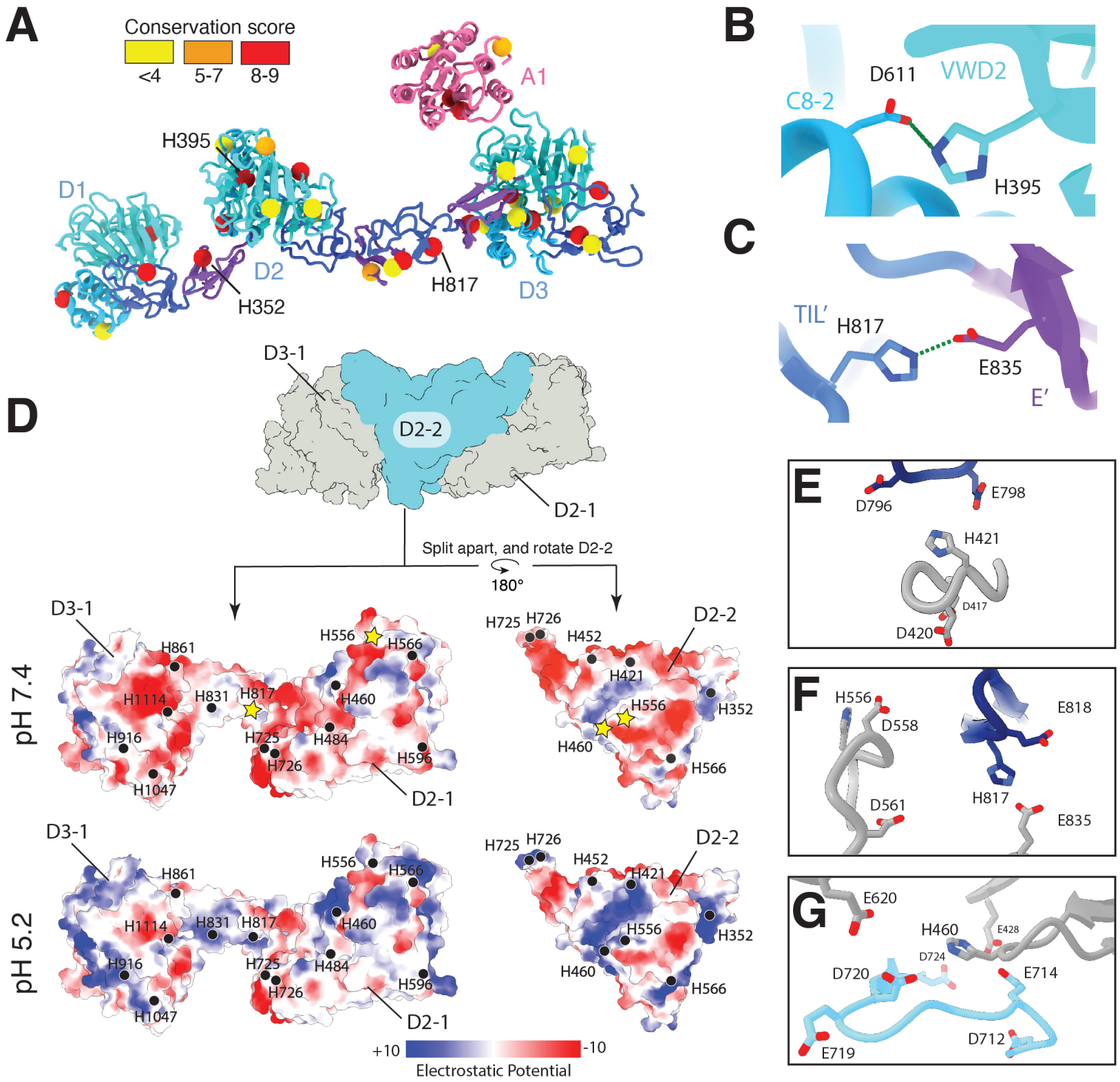

Figure 5

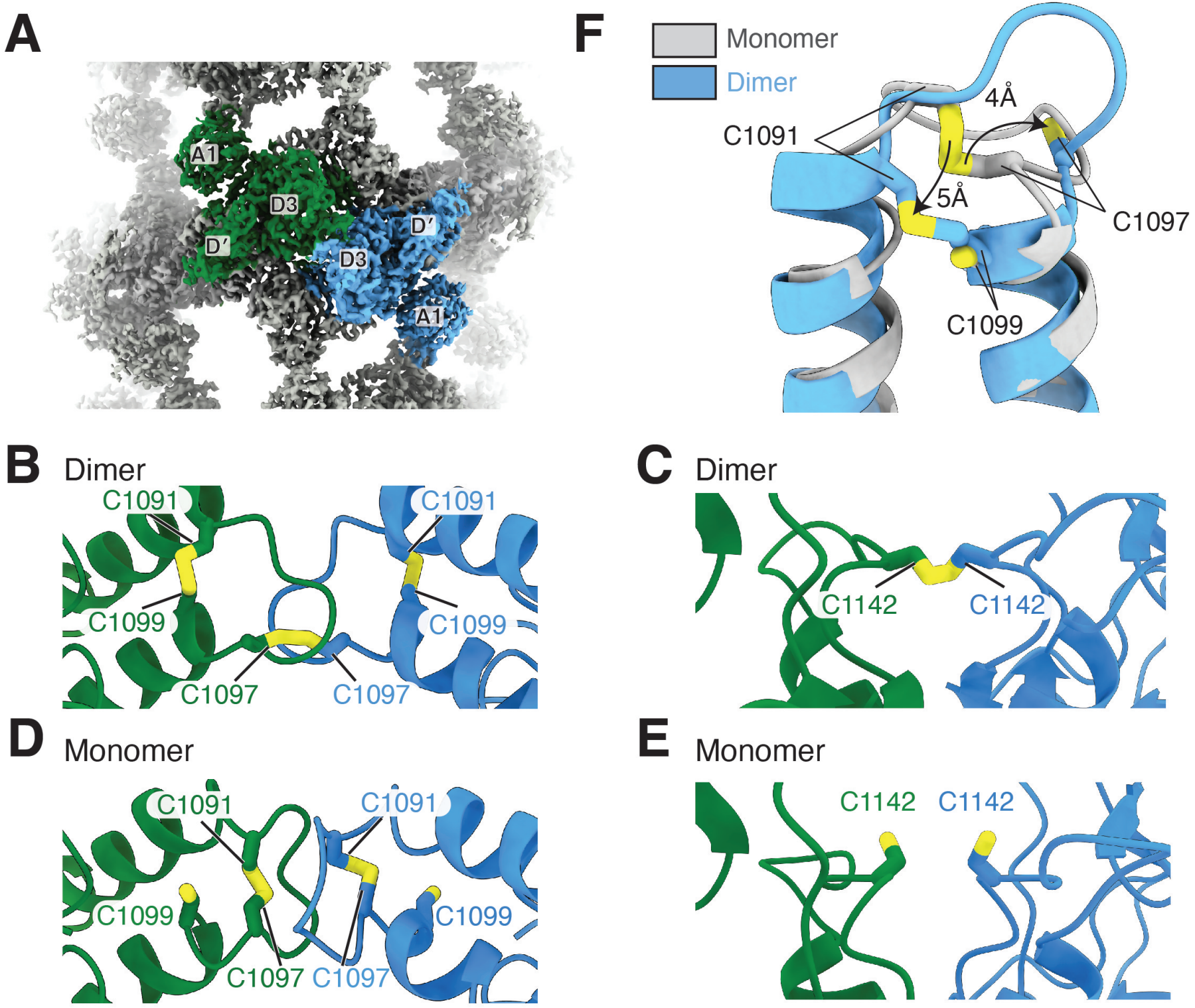

Figure 6

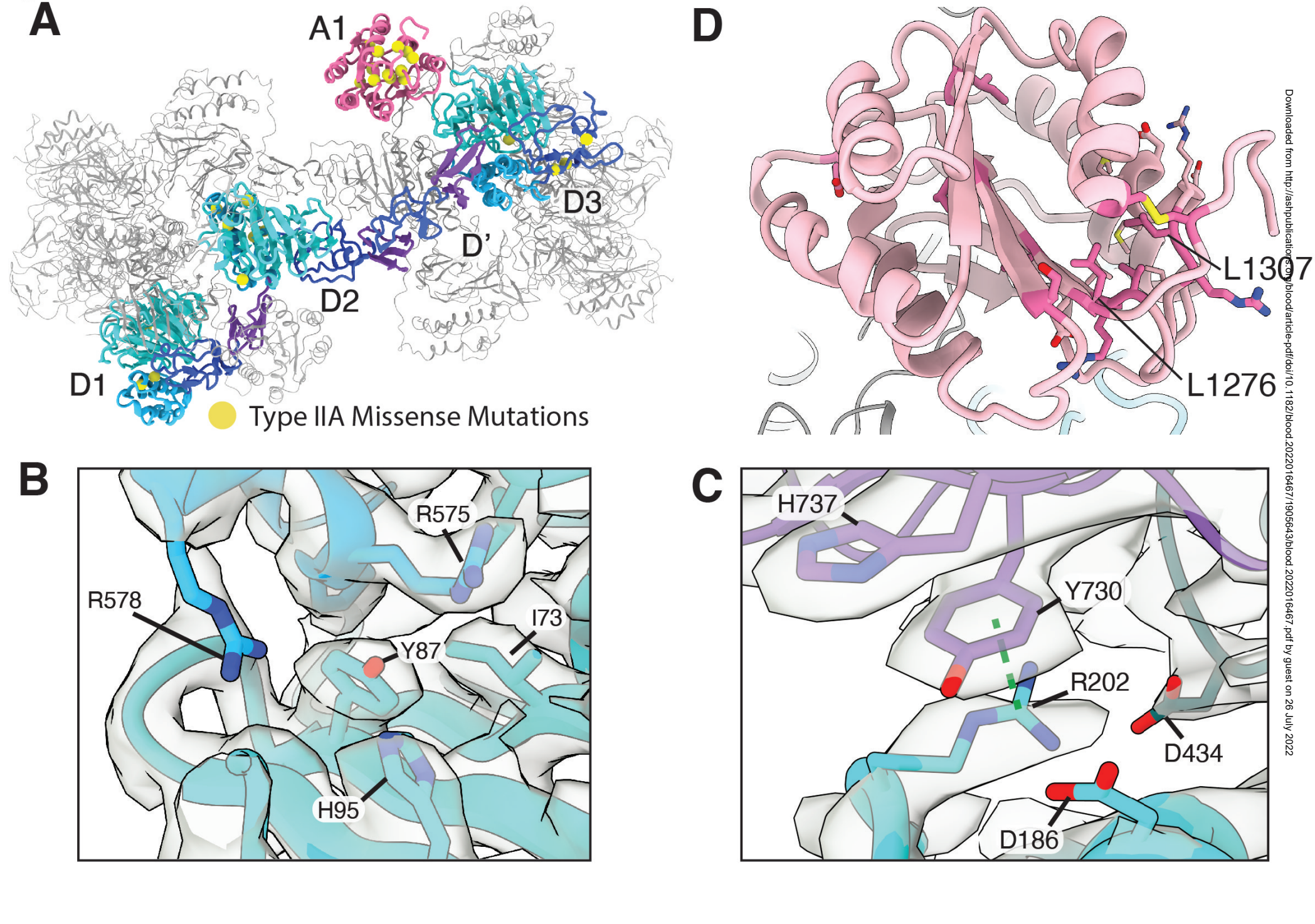

Figure 7

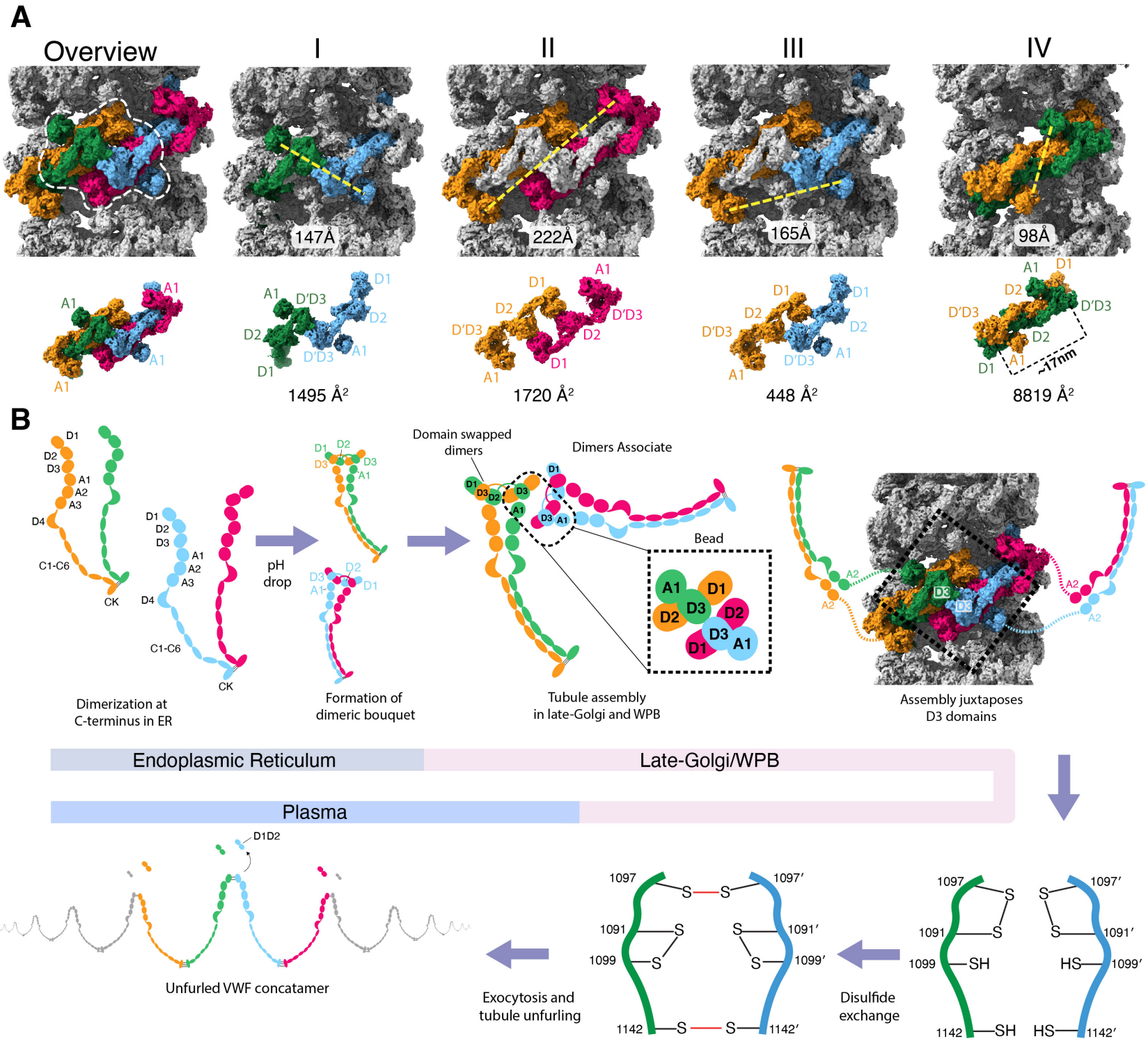

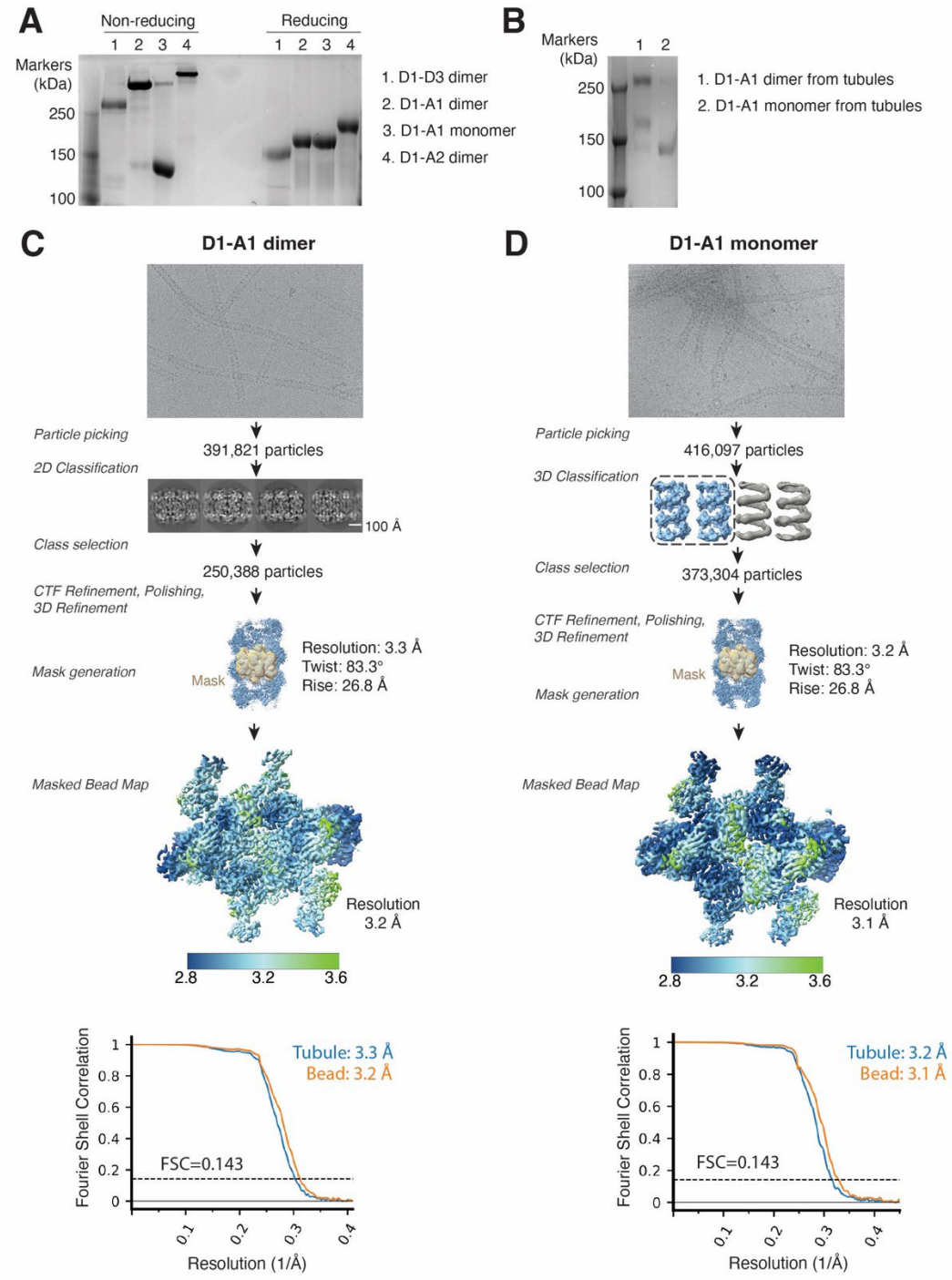

Figure S1. Cryo-EM processing. A. Purity of proteins used for tubule formation. All samples were run on a 5% SDS-PAGE gel. Samples on the right had a reducing agent in the loading buffer whereas samples on the left were run in non-reducing conditions to preserve their disulfide-bond linkages. **B**. Non-reducing SDS-PAGE analysis of proteins after tubules were formed demonstrate that tubule formation was insufficient to cause monomers to dimerize. **C**. Flow diagram of the cryo-EM processing steps used to

determine the structure of VWF tubules generated from the D1-A1 dimer. Below, Fourier shell correlation (FSC) curves for the tubule a central single bead, with the resolution at FSC=0.143 indicated. **D**. As C, but for VWF tubules generated from the D1-A1 monomer.

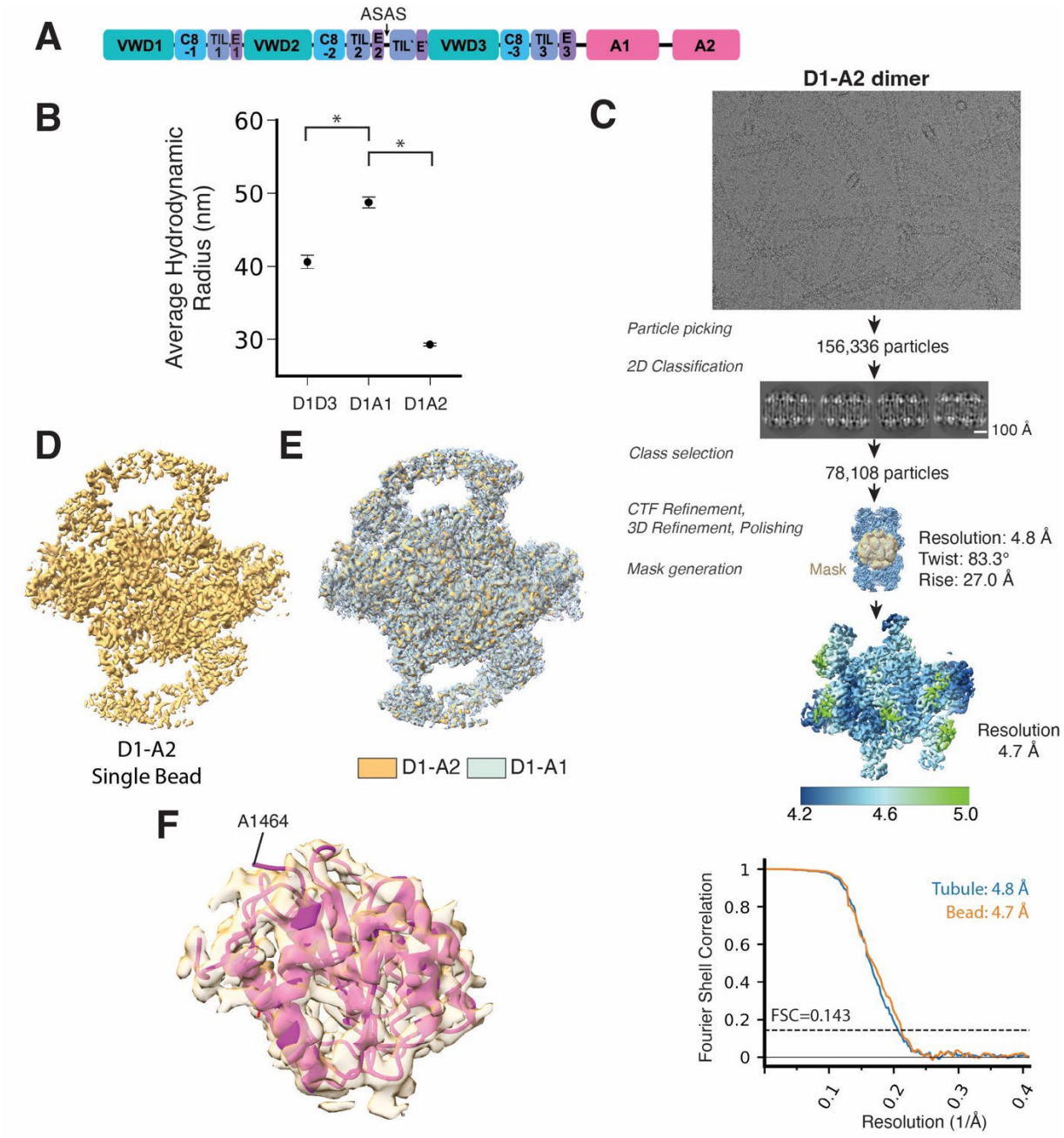

Figure S2. Cryo-EM processing of VWF tubules generated from a D1-A2 construct. A. Diagram of the D1-A2 construct. **B**. Hydrodynamic radius from dynamic light scattering (DLS) experiments of D1-D3, D1-A1, and D1-A2 after incubation at pH 5.2 for 24 hours. Error bars represent difference of the mean hydrodynamic radius across two replicates. Asterisks indicate two sample t-test p-value < 0.05. **C.** Flow diagram of the cryo-EM processing steps used to determine the structure of VWF tubules generated from purified D1-A2. Below, Fourier shell correlation (FSC) curves for the tubule and a single central bead, with the resolution at FSC=0.143 indicated. **D.** Density of a single D1-A2 bead. **E**. Overlay of the D1-A2 bead with transparent density from the D1-A1 dimer. No additional domains or domain

rearrangements are observed relative to the D1-A1 map. **F**. A1 model docked into the density of the A1 domain in D1-A2 tubules. No density is observed after residue A1464 for the A2 domain or linker to the A2 domain.

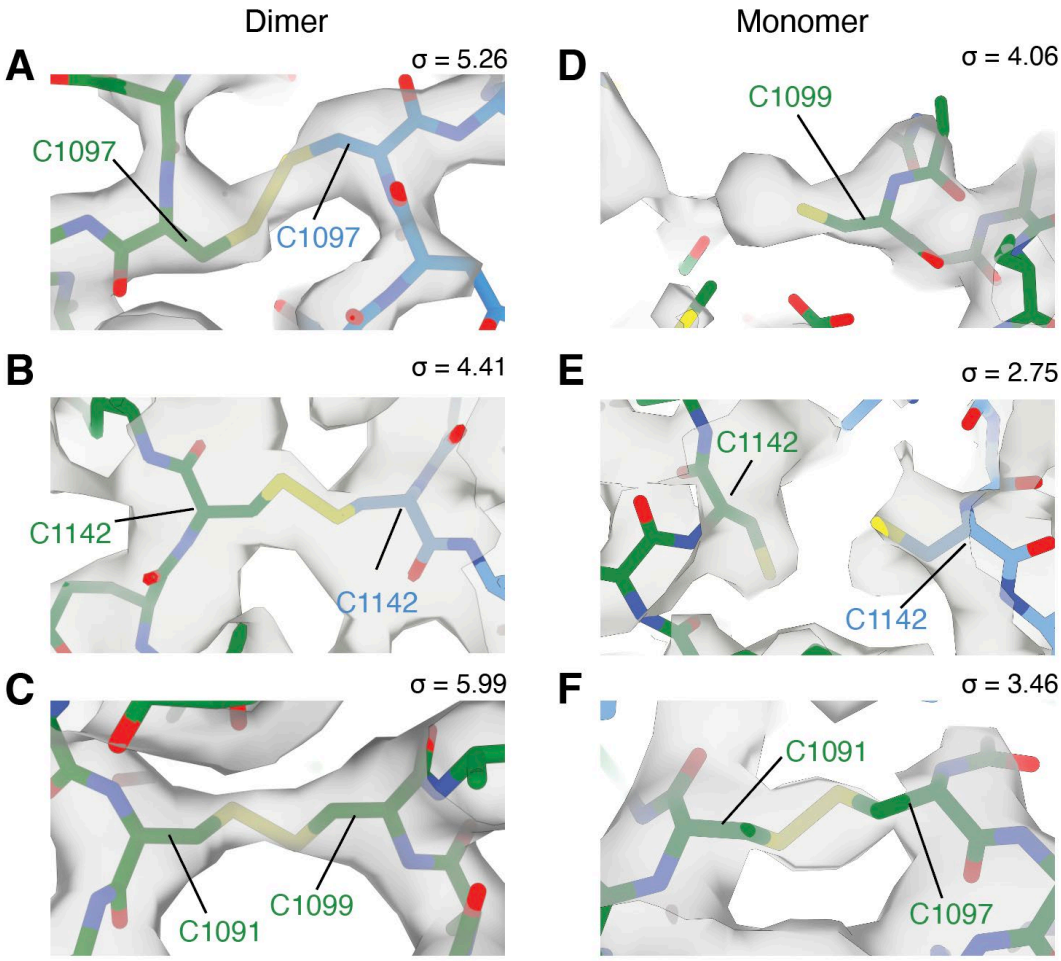

Figure S3. Cryo-EM map densities for mechanistically important cysteines and disulfide bonds. **A**. Density for the intermolecular C1097-C1097 disulfide bond in the D1-A1 dimer-derived tubule. **B**. Density for the intermolecular C1142-C1142 disulfide bond in the D1-A1 dimer-derived tubule. **C**. Density for the intramolecular C1091-C1099 disulfide bond in the D1-A1 dimer-derived tubule. **D**. Density for C1099 in the monomer-derived tubule. Unexplained density is seen adjacent to the sulfhydryl group. **E**. Density for C1142 in adjacent molecules in the monomer-derived tubule. **F**. Density for the intramolecular C1091-C1097 disulfide bond in the monomer-derived tubule. In all panels, the bonds are shown as sticks colored by element. Different molecules have carbons colored in green and blue, respectively. The cryo-EM maps were sharped with Phenix v1.19[22]. Contour level is indicated in the upper right of each panel.

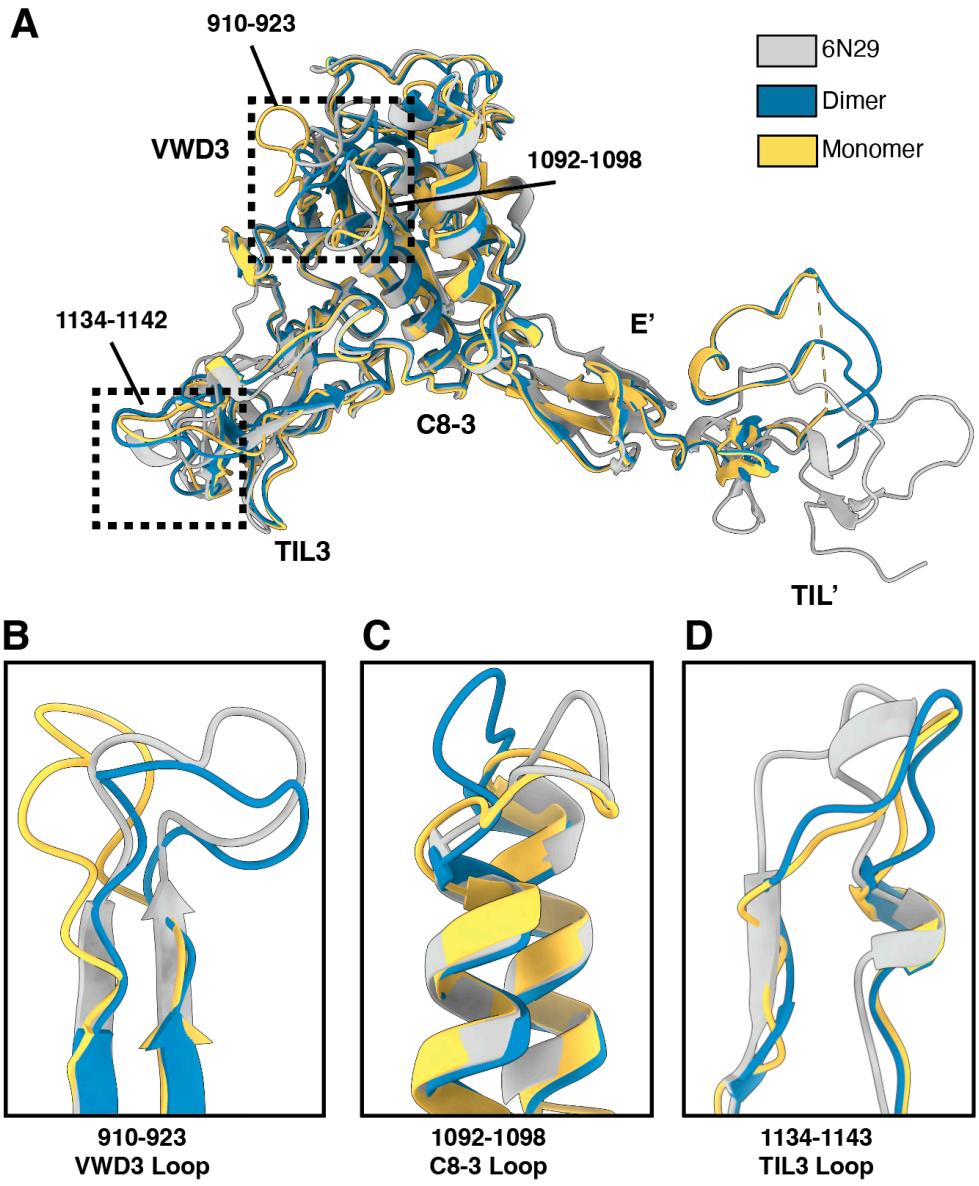

Figure S4. Superposition of atomic models of D′D3. **A.** Superposition of the D′D3 crystal structure (PDB: 6N29) [14] with atomic models determined from cryo-EM maps of VWF tubules assembled with either monomeric or dimeric D1-A1. The positions of interfacial loops highlighted in panels B-D are boxed. **B**. Superposition of the 910-923 loop. **C**. Superposition of the 1092-1098 loop. **D.** Superposition of the 1134-1143 loop. Superposition performed using the matchmake function of ChimeraX 1.3.

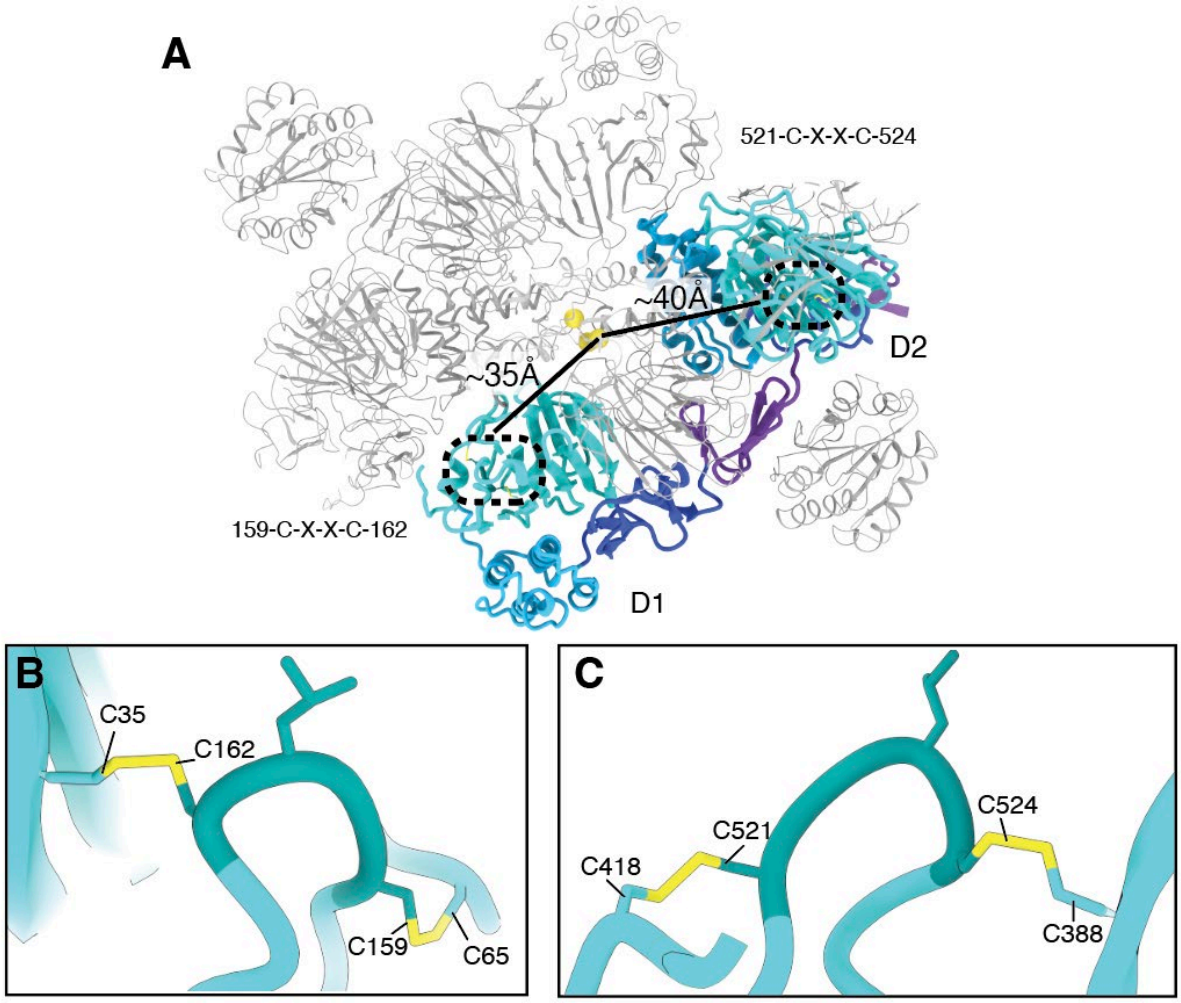

Figure S5. CXXC motifs in the prodomain are unlikely to catalyze disulfide exchange. **A**. Model of a single bead in grey with one D1 and D2 assembly colored by domain. Yellow spheres with 3 Å radius are placed at C1091, C1097, and C1099. Positions of CXXC motifs implicated in VWF intrinsic oxidoreductase activity[35] are denoted by dashed ellipses. The distance of each motif to C1099 is measured from the first cysteine. **B**. Atomic model depicting C159 and C162 of the D1 C159-XX-C162 motif in intramolecular disulfide bonds. **C**. Atomic model depicting C521 and C524 of the D2 C521-XX-C524 motif in intramolecular disulfide bonds.

Supplemental Video Legends

Movie S1. Overview of the VWF tubule showing the organization of the VWF D1-A1 domains. The A1 domain is a component of the tubule wall that links helical repeats. Distinct molecules are denoted by no apostrophe, one apostrophe (’), or two apostrophes (’’).

SUPPLEMENTAL TABLES

Table S1. Statistics for data collection, data processing, model refinement and validation.

	D1-A1 (monomer)	D1-A1 (dimer)	D1-A2 (dimer)
Data collection			
Microscope	Titan Krios	Titan Krios	Talos Artica
Detector	K3	K3	K3
Voltage (keV)	300	300	200
Nominal magnification	81,000	81,000	36,000
Electron exposure ($e^-/Å^2$)	55.52	55.46	53.06
Defocus range set during data acquisition (μm)	-0.6 to -2.0	-0.6 to -1.8	-1.2 to -2.2
Pixel size (Å)	1.06	1.06	1.1
Total movies acquired	12,996	6,121	1,065
Data Processing			
EMDB code	EMDB-27156	EMDB-27157	EMDB-27158
Particles	373,304	250,388	78,108
Helical Twist	83.3	83.3	83.3
Helical Rise	26.8	26.8	27.0
Map resolution (Å), Tubule Masked	3.2	3.3	4.8
Map resolution (Å), Single Bead Masked	3.1	3.2	4.7
Model composition			
PDB code	8D3C	8D3D	
Chains	16	16	
Atoms	162,720	163,856	
Residues	20,880	21,024	
Ligands	Ca^{2+}: 48, NAG: 80	$Ca^{2+:}$ 48, NAG: 80	
Refinement			
Resolution limit set in refinement (Å)	3.1	3.2	
Correlation coefficient (CCmask)	0.79	0.81	
C_{ref} (masked) (Å)	3.3	3.4	
Root-mean-square deviation (bond lengths) (Å)	0.004	0.007	
Root-mean-square deviation (bond angles) (Å)	1.125	1.042	
Validation			
MolProbity Score	1.05	1.17	
Clashscore	0.92	1.96	
Rotamer outliers (%)	0.35	0	
Ramachandran (favored) (%)	96.06	96.68	
Ramachandran (outliers) (%)	0	0	

Table S2. Analysis of VWF D1-A1 histidine residues. Structure-based analysis of all the histidine residues present in human VWF domains D1-A1 in the dimer-derived tubule structure. Conservation scores were determined using ConSurf [47]. pKa values were determined using pdb2pqr 3.4.1[48]. Abbreviations: WT = wild type.

Histidine	Location	Conser-vation Score	Structure-based pKa	Protonated upon pH drop (7.4 to 5.2)	Molecular environment	Effect of substitution on D1D3 dimerization[33]	Effect of substitution on VWF concatemerization [33]
95	VWD1	7	2.9	No	Near interface with C8-2 of neighbor. In an electronegative environment close to D75, D93 and D106.	Decreased	Slightly reduced
238	C8-1	7	5.7	Yes	Near interface with A1 domain.	WT levels	WT levels
288	C8-1	3	6.2	Yes	Faces solvent.		
316	TIL1	7	5.7	Yes	Near interface with VWD3 of neighbor.		
352	E1	9	3.8	No	Near interface with VWD3 of neighbor. Close to E1015 of neighbor.	WT levels	WT levels
395	VWD2	9	6.5	Yes	Potentially forms an intramolecular salt bridge with D611 of the C8-2 domain.	Prevented (H395A and H395R)	No concatemers (H395A or H395R/K)
421	VWD2	3	6.2	Yes	Faces solvent.		
452	VWD2	2	6.5	Yes	Near VWD2 of neighbor. May help neutralize charge of D467.		
460	VWD2	9	2.6	No	At interface with E2 of neighbor. Likely helps flanking R505 and K459 make salt bridges.	Prevented (H460L), Reduced (H460M/Q/A), Restored (H460R/K)	Impaired (H460A/L/M/Q) WT levels (H460K/R)
484	VWD2	4	5.4	Yes	7 Å from interface with VWD2 of neighbor.		
556	VWD2	5	5.5	Yes	In a histidine-rich region with H725/726 of neighboring molecule.		
566	C8-2	1	4.9	No	May interact with D437.		
596	C8-2	9	5.6	Yes	Near interface with C8-3 of neighbor. May interact with E593.	Decreased (H596A and H596R)	Reduced
725	E2	8	7.7	No	In a histidine-rich region.	WT levels	Impaired concatemerization
726	E2	3	6.3	Yes	In a histidine-rich region.		
737	E2	5	6.7	Yes	In an electronegative region at the interface with VWD1 of neighbor. Could neutralize electronegative charge.	Decreased (H737A and H737R)	Impaired concatemerization (H737A or H737R)
759	E2	5	-	-	Not resolved.		
817	TIL'	7	6.9	Yes	Potentially form intramolecular salt bridge with E835 of the E′ domain.		
831	TIL'	9	4.4	No	Potentially interacts with E543 of neighboring VWD2 domain. May form a water bridge with H1114.	WT levels	WT levels
861	TIL'	2	6.3	Yes	Faces solvent.		

874	VWD3	9	2.2	No	Likely coordinates a water molecule.	WT levels	WT levels
916	VWD3	3	5.2		On a flexible loop.		
952	VWD3	3	6.6	Yes	Potentially forms a salt bridge with E930 of same molecule.		
977	VWD3	3	5.8	Yes	In an electronegative environment surrounded by D975, D1096, and D1102.		
1047	C8-3	2	6.9	Yes	Potentially interacts with D1040,		
1109	C8-3	7	4.1	No	Forms intramolecular contacts.		
1114	C8-3	1	5.3	Yes	Potentially forms a water bridge with H831.		
1159	TIL3	9	6.6	Yes	May neutralize charge of acidic residues at the intramolecular interface with VWD3.	Impaired secretion	
1174	TIL3	8	5.0	No	Near glycosylation.	WT levels	WT levels
1176	TIL3	1	6.2	Yes	Near glycosylation.		
1221	E3	2	-	-	Not resolved	Reduced	WT levels
1226	E3	6	-	-	Not resolved	WT-levels	Reduced
1268	A1	6	6.0	Yes	Faces solvent		
1322	A1	8	3.8	No	At interface with E1. Forms a potential water bridge with H1326.		
1326	A1	7	3.1	No	At interface with E1. Forms a potential water bridge with H1322.		
1419	A1	3	5.8	Yes	Faces solvent		

Table S3. Analysis of single-residue substitutions associated with type 2A VW disease.
Abbreviations: HWM, high molecular weight; ER, endoplasmic reticulum; WPBs, Weibel-Palade bodies.

Mutation	Observations from structure	Evidence from literature
R202W	At interface between 3 molecules. Forms cation-π interactions with Y730 of neighboring E2 domain and electrostatic interactions with D168 and D434. A tryptophan substitution would disrupt electrostatic interactions but maintain stacking interactions.	Reduced HMW concatemers[38]
R273W	Likely forms an intramolecular salt bridge with D141 that would be lost by a substitution to tryptophan.	Patients lacked HMW concatemers in plasma. Mutation increased ER retention of recombinant VWF in COS-7 cells[49].
N528S	Involved in coordinating calcium. Loss may lead to a disruption of the calcium-binding site, which occurs at the VWD2-VWD3 interface.	Patients lack HMW concatemers. N528S-VWF variant showed only diffuse staining consistent with no WPBs. Increased ER retention[50].
G550R	An arginine substitution would affect intramolecular packing by generating a clash with F406.	Decreased levels of HMW concatemers[51]. Did not form WPBs potentially because of a secretion defect[52].
S979N	May disrupt intramolecular packing.	S979N might be associated with VW disease type 2E[53].
G1180R	Faces solvent. Substitution may decrease local structural flexibility.	Reduced HMW concatemers but not replicated with recombinant VWF protein secreted into media[54].
L1276P	Could prevent proper folding of the hydrophobic core of the A1 domain.	Patients lacked HMW concatemers in plasma[40].
V1279F	Could prevent proper folding of the hydrophobic core of the A1 domain.	Absence of HMW concatemers[55].
L1307P	Could prevent proper folding of the hydrophobic core of the A1 domain.	Marginal decrease of the largest VWF concatemers. Reduced production and increased ER retention. Mainly short/round WPBs[39].
V1316M	Could prevent proper folding of the hydrophobic core of the A1 domain.	Reduced HMW concatemers[56]. Also associated with severe thrombocytopathy[57].
R1374H	May affect folding of the A1 domain.	Reduced HMW concatamers.[58]